












# Cryo-EM structure of the human NKCC1 transporter reveals mechanisms of ion coupling and specificity

Caroline Neumann<sup>1,2</sup> , Lena Lindtoft Rosenbæk<sup>3</sup> , Rasmus Kock Flygaard<sup>1,2</sup> , Michael Habeck<sup>1,2</sup> , Jesper Lykkegaard Karlsen<sup>2</sup>, Yong Wang<sup>4,5</sup> , Kresten Lindorff-Larsen<sup>4</sup> , Hans Henrik Gad<sup>2</sup> , Rune Hartmann<sup>2</sup> , Joseph Anthony Lyons<sup>1,2,6</sup> , Robert A Fenton<sup>3,\*</sup>  & Poul Nissen<sup>1,2,\*\*</sup> 

## Abstract

The sodium–potassium–chloride transporter NKCC1 of the SLC12 family performs Na<sup>+</sup>-dependent Cl<sup>-</sup> and K<sup>+</sup>-ion uptake across plasma membranes. NKCC1 is important for regulating cell volume, hearing, blood pressure, and regulation of hyperpolarizing GABAergic and glycinergic signaling in the central nervous system. Here, we present a 2.6 Å resolution cryo-electron microscopy structure of human NKCC1 in the substrate-loaded (Na<sup>+</sup>, K<sup>+</sup>, and 2 Cl<sup>-</sup>) and occluded, inward-facing state that has also been observed for the SLC6-type transporters MhsT and LeuT. Cl<sup>-</sup> binding at the Cl1 site together with the nearby K<sup>+</sup> ion provides a crucial bridge between the LeuT-fold scaffold and bundle domains. Cl<sup>-</sup>-ion binding at the Cl2 site seems to undertake a structural role similar to conserved glutamate of SLC6 transporters and may allow for Cl<sup>-</sup>-sensitive regulation of transport. Supported by functional studies in mammalian cells and computational simulations, we describe a putative Na<sup>+</sup> release pathway along transmembrane helix 5 coupled to the Cl2 site. The results provide insight into the structure–function relationship of NKCC1 with broader implications for other SLC12 family members.

**Keywords** cation:chloride cotransporters; chloride transport; ion coupling; ion sites; NKCC1

**Subject Category** Structural Biology

**DOI** 10.15252/embj.2021110169 | Received 10 November 2021 | Revised 20 September 2022 | Accepted 22 September 2022 | Published online 14 October 2022

**The EMBO Journal (2022) 41: e110169**

## Introduction

Eukaryotic cation:chloride cotransporters (CCCs) encompass the SLC12 family and can be divided into three subclasses: the Na<sup>+</sup>:K<sup>+</sup>:2Cl<sup>-</sup> (NKCCs, SLC12A1-2), Na<sup>+</sup>:Cl<sup>-</sup> (NCC, SLC12A3), and K<sup>+</sup>:Cl<sup>-</sup> (KCCs, SLC12A4-7) cotransporters. Furthermore, there are two orphan transporters CCC9 (SLC12A8) and CIP1 (SLC12A9; Arroyo *et al*, 2013). The Cl<sup>-</sup> translocation by CCCs is secondary active, driven by Na<sup>+</sup> or K<sup>+</sup> gradients established by the plasma membrane Na<sup>+</sup>-K<sup>+</sup>-ATPase (Payne, 2012; Markadieu & Delpire, 2014). NKCCs transport K<sup>+</sup> and Cl<sup>-</sup> into cells coupled to Na<sup>+</sup> influx and NCC cotransports Na<sup>+</sup> and Cl<sup>-</sup> into cells, whereas KCCs extrude K<sup>+</sup> and Cl<sup>-</sup> out of cells (Hebert *et al*, 2004). All the characterized cotransporters are electroneutral and are important for maintaining cellular Cl<sup>-</sup> balance and cell volume in numerous different cell types (Delpire & Gagnon, 2018). NCC and NKCC2 activity in the kidney is important for the maintenance of NaCl homeostasis and, hence, blood pressure regulation (Arroyo *et al*, 2013), with NKCC2 also important for NH<sub>4</sub><sup>+</sup> reabsorption and acid–base homeostasis (Markadieu & Delpire, 2014). Maintenance of cellular Cl<sup>-</sup> balance by CCCs in the central nervous system is not only important for neuronal proliferation and differentiation but it also determines the strength of inhibitory, hyperpolarizing neurotransmission by glycine- and GABA-gated Cl<sup>-</sup> channels, respectively (Blaesse *et al*, 2009). NKCC1 inhibits the L-amino acid transporter LAT1 and Akt/Erk pathways and mTORC1 activation (Demian *et al*, 2019), thereby creating a connection between cell volume and cell mass regulation. The importance of CCCs is highlighted by numerous diseases associated with an improper function such as epilepsy, neuropathic pain, anxiety, cerebral ischemia, autism, and schizophrenia (Jaggi *et al*, 2015). Inactivating mutations of NKCC2 lead to type I Bartter's syndrome (Simon *et al*, 1996a) and mutations of NCC cause Gitelman syndrome

1 Danish Research Institute of Translational Neuroscience—DANDRITE, Nordic EMBL Partnership for Molecular Medicine, Aarhus, Denmark

2 Department of Molecular Biology and Genetics, Aarhus University, Aarhus, Denmark

3 Department of Biomedicine, Aarhus University, Aarhus, Denmark

4 Linderstrøm-Lang Centre for Protein Science, Department of Biology, University of Copenhagen, Copenhagen, Denmark

5 Shanghai Institute for Advanced Study, Institute of Quantitative Biology, College of Life Sciences, Zhejiang University, Hangzhou, China

6 Interdisciplinary Nanoscience Center (iNANO), Aarhus University, Aarhus, Denmark

\*Corresponding author. Tel: +45 28992149; E-mail: robert.a.fenton@biomed.au.dk

\*\*Corresponding author. Tel: +45 28992295; E-mail: pn@mbg.au.dk

(Simon *et al.*, 1996b; Ji *et al.*, 2008), both characterized by reduced  $K^+$  and elevated pH levels in the blood. Mutations of KCC3 cause Andermann syndrome, a severe neurodegenerative disorder (Arroyo *et al.*, 2013). NKCC1 mutations are also linked to impaired hearing and neurodevelopment (Koumangoye *et al.*, 2021).

Recently, cryo-EM structures of the dimeric NKCC1 (Chew *et al.*, 2019; Yang *et al.*, 2020; Zhang *et al.*, 2021), KCC1 (Liu *et al.*, 2019; Chi *et al.*, 2021a), KCC2 (Xie *et al.*, 2020; Chi *et al.*, 2021b), KCC3 (Xie *et al.*, 2020; Chi *et al.*, 2021a), and KCC4 (Xie *et al.*, 2020) transporters as well as a monomeric structure of KCC4 (Reid *et al.*, 2020) have described the three-dimensional architecture of these transporters, their fold, and the potential localization of their ion-binding sites. All these structures present the transporters in their partially occluded inward-facing conformation with substrates still occupying the binding pockets, although the  $Na^+$  sites remain undetermined. They contain 12 transmembrane (TM) helices with an inverted pseudo-twofold symmetry between TM1-5 and TM6-10, first identified as the LeuT fold (Yamashita *et al.*, 2005). TM helices 1 and 6 contain non-helical junctions in the middle that allows for independent movement of the intracellular and extracellular halves to expose or close the substrate-binding sites to solvent access in an “alternating access” mechanism (Joseph *et al.*, 2019). Despite coming from two distinct vertebrates with only 74% sequence identity, the  $K^+$ - and  $Cl^-$ -binding sites in zebrafish (*Danio rerio*, zNKCC1) and human NKCC1 (hNKCC1) are fully conserved, highlighting the importance of specific residues for interacting with the transported ions. The regulatory N-terminal domain in hNKCC1 is disordered in nature (Chew *et al.*, 2019; Yang *et al.*, 2020). Crystal structures of the regulatory C-terminal domain of a bacterial NKCC1 homolog (Warmuth *et al.*, 2009) and the eukaryotic C-terminal domain of KCC1 have provided further insight into the regulatory mechanisms of CCC transporters (Zimanyi *et al.*, 2020).

Sharing the LeuT-fold (Chew *et al.*, 2019; Yang *et al.*, 2020; Zhang *et al.*, 2021), NKCC1, and SLC6 transporters also have mechanistic aspects of their  $Na^+$ -dependent function in common. Since the first LeuT crystal structure (Yamashita *et al.*, 2005), other SLC6 structures have been determined in a variety of different conformational states and in complexes with substrates or inhibitors including *Bacillus halodurans* amino acid transporter MhsT (Malinauskaite *et al.*, 2014), fruit fly dopamine transporter dDAT (Penmatsa *et al.*, 2013), human serotonin transporter SERT (Coleman *et al.*, 2016), amino acid transporter B<sup>0</sup>AT1 (Yan *et al.*, 2020), and glycine transporter GlyT (Shahsavari *et al.*, 2021). LeuT-fold transporters contain two domains: the bundle domain comprising TM 1–2 and TM 6–7 that performs the main conformational changes throughout the transport cycle, and the scaffold domain encompassing TM 3–4 and TM 8–9 that stays almost rigid throughout the functional cycle. This is often referred to as a rocking-bundle mechanism (Forrest & Rudnick, 2009; Forrest *et al.*, 2011). Ligand- and ion-binding sites are localized at the interface of the scaffold and bundle domain and binding/release of specific ligands controls bundle movements and coupling (Zhang *et al.*, 2018). For SLC6 transporters, binding of extracellular  $Na^+$  at the Na2 site (corresponding to the expected  $Na^+$ -binding site of NKCC1) stabilizes outward-facing states, followed by subsequent binding of substrates at S1 and Na1 sites. The  $Na^+$  and substrate-bound state can then explore conformational changes toward the inward-facing state (Ben-Yona & Kanner, 2009; Claxton *et al.*, 2010; Zhao *et al.*, 2010; Fenollar-Ferrer *et al.*, 2014; Kazmier

*et al.*, 2014; Tavoulari *et al.*, 2016), where  $Na^+$  release from the Na2 site to the cytoplasm (Malinauskaite *et al.*, 2014) leads further to the inward-open state with substrate release from the S1 and Na1 sites (Krishnamurthy & Gouaux, 2012). The main substrate alone has no effect on the conformational state without  $Na^+$  ions present, and the Na2 site is a crucial structural element for cytoplasmic occlusion and opening (Tavoulari *et al.*, 2016).

Here, we present a 2.6 Å resolution cryo-EM structure of the transmembrane unit of the human NKCC1 cotransporter with bound  $K^+$ , two  $Cl^-$ , and  $Na^+$  ions. The higher-resolution map reveals important details of substrate- and lipid-binding sites and the functional state that pose important questions on transport mechanisms, which we address through functional studies and MD simulations.

## Results

### NKCC1 cryo-EM determination

We collected cryo-EM data of hNKCC1 and performed single-particle analysis, which resulted in a 2.6 Å resolution 3D reconstruction of the transmembrane domain of human NKCC1 in its occluded, inward-facing, substrate-bound conformation (Fig 1A and Appendix Table S1). In three individual data sets, single-particle images were extensively cleaned through multiple rounds of 3D classification before high-resolution reconstructions were obtained from 3D auto-refinement of Bayesian polished particles. Inspection of the reconstructions from the individual data sets revealed the same state of hNKCC1, thus we merged data into a single stack of 256,791 particle images to obtain a higher-quality reconstruction (Figs EV1–EV4 and EV5A). Similar to other NKCC1 cryo-EM structures (Chew *et al.*, 2019; Yang *et al.*, 2020; Zhang *et al.*, 2021), the N-terminal domain could not be identified on the map. The regulatory cytoplasmic domain (aa 756–1212) appears to be flexible and, despite extensive attempts for classification in cryoSPARC (Punjani *et al.*, 2017) and the use of multibody refinement in RELION (Nakane *et al.*, 2018), it appeared only at a local resolution of 7–8 Å (Fig 1A). However, it confirmed an overall asymmetric configuration of the transmembrane domains (Figs 1A and EV4A–C). The cytoplasmic domains were masked out along with the detergent micelle and the refinement was focused on the transmembrane part of the transporter (Figs EV1–EV3). The LeuT-fold topology and the dimeric architecture of the transmembrane region of hNKCC1 are presented in Fig 1B and Appendix Fig S2A.

The final map for the transmembrane domain was of sufficient quality to clearly identify non-protein features corresponding to lipids, sterols, a  $K^+$  ion, a  $Na^+$  ion, and two  $Cl^-$  ions. When compared to the well-characterized SLC6-type amino acid transporters LeuT (Gotfryd *et al.*, 2020) and MhsT (Malinauskaite *et al.*, 2014), it is clear that despite different substrates, the binding sites are similar and overlap. Hence, the models for  $Na^+$ -coupled transport in SLC6 and SLC12 transporters appear mutually informative.

### Lipid and cholesterol binding to hNKCC1

Similar to zNKCC1 (Chew *et al.*, 2019), our three-dimensional EM map revealed the presence of seven lipid molecules bound at the central cleft with either one or both acyl chains inserted between the

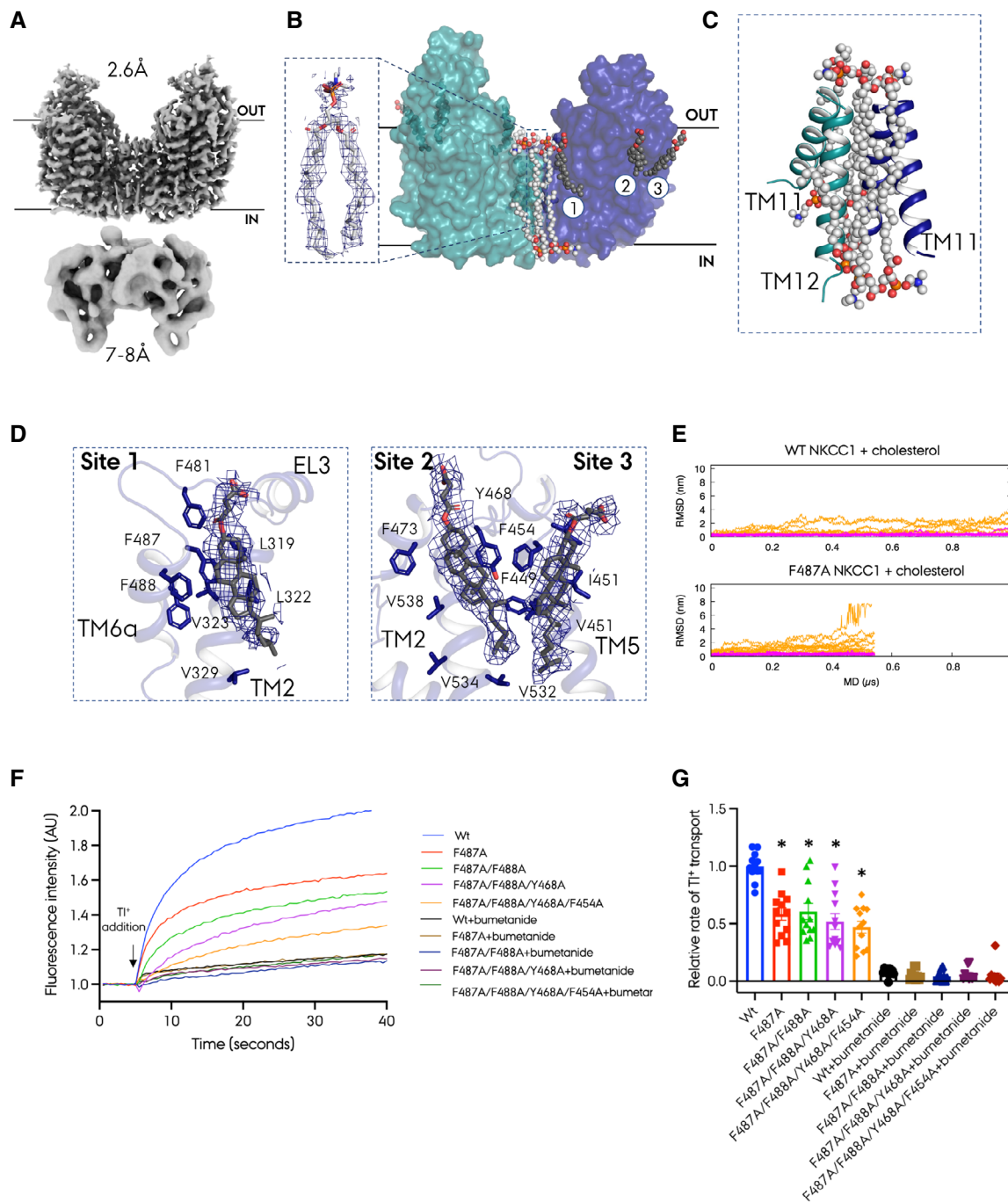


**Figure 1. Overview of the hNKCC1 structure.**

A EM density of the transmembrane domain of hNKCC1 (resolved to 2.6 Å) and the cytoplasmic domain (resolved to 7–8 Å).

B Surface representation of the transmembrane domain of NKCC1 with lipid molecules localized at the dimerization interface (shown in spheres) and the three cholesterol-binding sites (shown in spheres) per protomer. In the inset, a representative EM density for a lipid molecule is presented.

C TM11 and TM12 from each protomer are presented together with the lipid molecules (shown in spheres) present at the dimerization interface.

D Densities for cholesterol molecules bound at cholesterol-binding sites 1, 2, and 3 are presented together with the modeled cholesterol hemisuccinate molecules.

E RMSD of wt NKCC1 and F487A NKCC1 dimer with cholesterol bound during the MD simulation. RMSD was calculated as deviations from the initial model at 0 μs.

F, G (F) Transport kinetics and (G) relative initial transport rates of wild-type hNKCC1 and hNKCC1 with mutations within the cholesterol-binding sites: F487A (site 1), F487A/F488A (site 1), F487A/F488A/Y468A (site 1 + 2), and F487A/F488A/Y468A/F454A (site 1 + 2 + 3) with and without addition of bumetanide; mean ± SEM,  $n = 3$  independent experiments with 4–6 replicates for each time point per experiment. In example of individual traces, fluorescence intensity is normalized to the average initial baseline period (without  $\text{Ti}^+$ ) for each individual cell line. Transport rates are normalized to individual NKCC1 expression per cell line and subsequently normalized to wild-type NKCC1 without bumetanide.

Source data are available online for this figure.

two protomers (Fig 1B and C). One lipid is placed directly on the C2 symmetry axis, whereas the remaining lipid molecules cluster in two pairs of three annular lipids found on opposite sides of the interface.

The EM map identified three cholesterol-binding sites per NKCC1 protomer at the transporter surface, corresponding to the outer leaflet of the plasma membrane (Fig 1D). We modeled them as cholesteryl hemisuccinate molecules (CHS), which were used in the solubilization and purification. The first CHS molecule was found close to the dimer interface, binding at a groove formed between TM2 and TM6a with its  $\alpha$ -face forming a  $\pi$ - $\pi$  interaction with F487 on TM6a (as well as other aromatic residues F488 and F491). In addition, F481 on EL3 and hydrophobic residues on TM2 (L319, L322, V323, and V329) interact (Fig 1D). The second CHS molecule interacts with hydrophobic residues on TM2 (V532, V534, and V538), TM5 (F449, V450, and F454), and F473 on EL3 and it forms a  $\pi$ - $\pi$  interaction with Y468 on EL3 (Fig 1D). A third and slightly less defined CHS site was observed in close proximity and interacting with the second CHS molecule, and V450, I451, and F454 on TM5 (Fig 1D). To investigate the stability of the modeled CHS sites 1 and 2, we performed molecular dynamics (MD) simulations of the transmembrane domain of our NKCC1 structure embedded into a mixed lipid bilayer consisting of phosphatidylcholine (POPC)/phosphoethanolamine (POPE)/cholesterol at a ratio of 2:2:1 over 1,000 ns (4 replicas). Indeed, both cholesterol molecules are stably bound, although site 2 is more rigidly bound than site 1. Mutation of F487 to an alanine destabilizes the binding of cholesterol at site 1, however, not enough to completely prevent cholesterol binding (Fig 1E and Movie EV1).

The CHS molecules appear to stabilize the inward-facing conformation of NKCC1, potentially having an effect on NKCC1 function. To examine this, we performed  $\text{Ti}^+$  influx experiments (mimicking  $\text{K}^+$  uptake) in mammalian cells expressing the wild-type hNKCC1 and various hNKCC1 mutants with alterations in the amino acid residues within predicted cholesterol-binding sites. The relative  $\text{Ti}^+$  influx of F487A (cholesterol site 1) is roughly 40% lower than that of the wild-type construct (Fig 1F and G). Constructs containing additional destabilizing mutations within the three cholesterol sites, F487A/F488A (site 1), F487A/F488A/Y468A (site 1 + 2), and F487A/F488A/Y468A/F454A (site 1 + 2 + 3), did not statistically significantly lower the  $\text{Ti}^+$  influx rate further. As an alternative approach, we measured  $\text{Ti}^+$  uptake in WT NKCC1-expressing cells after sequestering cholesterol in the plasma membrane using non-cell-permeable methyl- $\beta$ -cyclodextrin (M $\beta$ CD). This approach resulted in increased  $\text{Ti}^+$  uptake at lower extraction levels, commensurate with higher NKCC1 activity in the plasma membrane (Appendix Fig S1), whereas at higher extraction levels, still below cytotoxic levels, NKCC1 activity is lower relative to controls.

Comparison of unmodeled densities from the deposited KCC3 cryo-EM structure (Chi *et al*, 2021b), also adopting an inward-facing state, revealed that all three cholesterol-binding sites are conserved, despite low sequence conservation. Additionally, KCC3 seems to contain a fourth cholesterol-binding site that was not found in our NKCC1 cryo-EM maps (Appendix Fig S2E).

### **$\text{Na}^+$ -ion-binding site and its role in ion coupling**

In hNKCC1, the  $\text{Na}^+$  ion is coordinated by the main chain carbonyl oxygen of W300 and L297 on TM1 of the bundle domain, the

side-chain hydroxyl groups of S613 and S614, and the main chain carbonyl oxygen of A610 on TM8 of the scaffold domain (Fig 2A). Previously, the zNKCC1 and hNKCC1 structures were described as inward open or partially inward open (Chew *et al*, 2019; Yang *et al*, 2020; Zhang *et al*, 2021). However, we consider our structure as an occluded, inward-oriented conformation—i.e., a trapped intermediate immediately preceding  $\text{Na}^+$  release and subsequent  $\text{K}^+$  and  $\text{Cl}^-$  release to the cytoplasmic environment, analogous to structures of SLC6 transporters MhsT and LeuT of that state (Malinauskaite *et al*, 2014; Gotfryd *et al*, 2020). We observe a clear candidate release pathway for  $\text{Na}^+$  that extends from the  $\text{Na}^+$ -binding site to the cytoplasm along TM5. This pathway mediates the critical, first encounter of the  $\text{Na}^+$  site with the low- $\text{Na}^+$  cytoplasmic environment. Defining the dynamics and functional properties of this pathway, and how it compares to the  $\text{Na}^+$  independent transporters (Fig 2), is important for understanding NKCC1 transport activity.

Water molecules are found within the intracellular vestibule, however, the bound  $\text{Na}^+$  ion is not solvated (Fig 2A). The MOLE2.5 program was used to identify and analyze potential intracellular exit pathways (Berka *et al*, 2012; Fig 2B), as also addressed previously for a lower-resolution study of hNKCC1<sup>K289N\_G351R</sup> (Yang *et al*, 2020). Interestingly, intracellular pathway 1 is lined by E429 and E431 (predicted pKa values of 4.6 and 4.5 by PROPKA, i.e., both negatively charged at pH 7.5) at the cytoplasmic interface (Fig 3A). These residues are conserved in hNKCC1, hNKCC2, and hNCC, but absent in the  $\text{Na}^+$  independent KCC transporters (Fig 3B). Thus, they may act as internal “gatekeepers” that guide the  $\text{Na}^+$  ion from the binding site into the cytoplasmic environment. To probe a putative role of E429 and E431 in  $\text{Na}^+$  release for hNKCC1,  $\text{Ti}^+$  influx experiments were performed with various hNKCC1 mutants. The relative rate of  $\text{Ti}^+$  influx was significantly lower for E429A, E431A, and E431Q mutants when compared to wild-type hNKCC1. Additionally, there was no statistically significant difference between the relative transport rates of E431A (mutation to a non-polar residue without a negative charge) and E431Q mutants (mutation to a polar, isosteric residue without a negative charge; Fig 3C and D). Cell surface expression of wild-type hNKCC1 and these mutants were similar, indicating that the altered activity is not due to the altered association of the mutant protein with the plasma membrane (Fig EV5). MD simulations also implicate these residues (Fig 3E, see below). Together, the results suggest important roles of E429 and E431 in hNKCC1 activity.

Our hNKCC1 structure also reveals interactions between R294 on TM1a and Q435 on TM5 at the end of the putative  $\text{Na}^+$ -release pathway that partially closes off the intracellular side of the transporter and stabilizes the transporter in an occluded state (Fig 3A). These arginine and glutamine residues in hNKCC1 are also exclusively conserved in  $\text{Na}^+$ -dependent CCCs, suggesting that they are important for control of  $\text{Na}^+$ -dependent transport (Fig 3B). Consistent with this model, a R294A mutant has reduced transport activity relative to wild-type NKCC1 (Yang *et al*, 2020). Additionally, K289 located on TM1 is conserved in the  $\text{Na}^+$ -dependent CCCs, providing a potential interaction partner for one of the two conserved glutamate residues on TM5 in outward-facing conformational states, where the intracellular side would be fully sealed (Fig 3B).

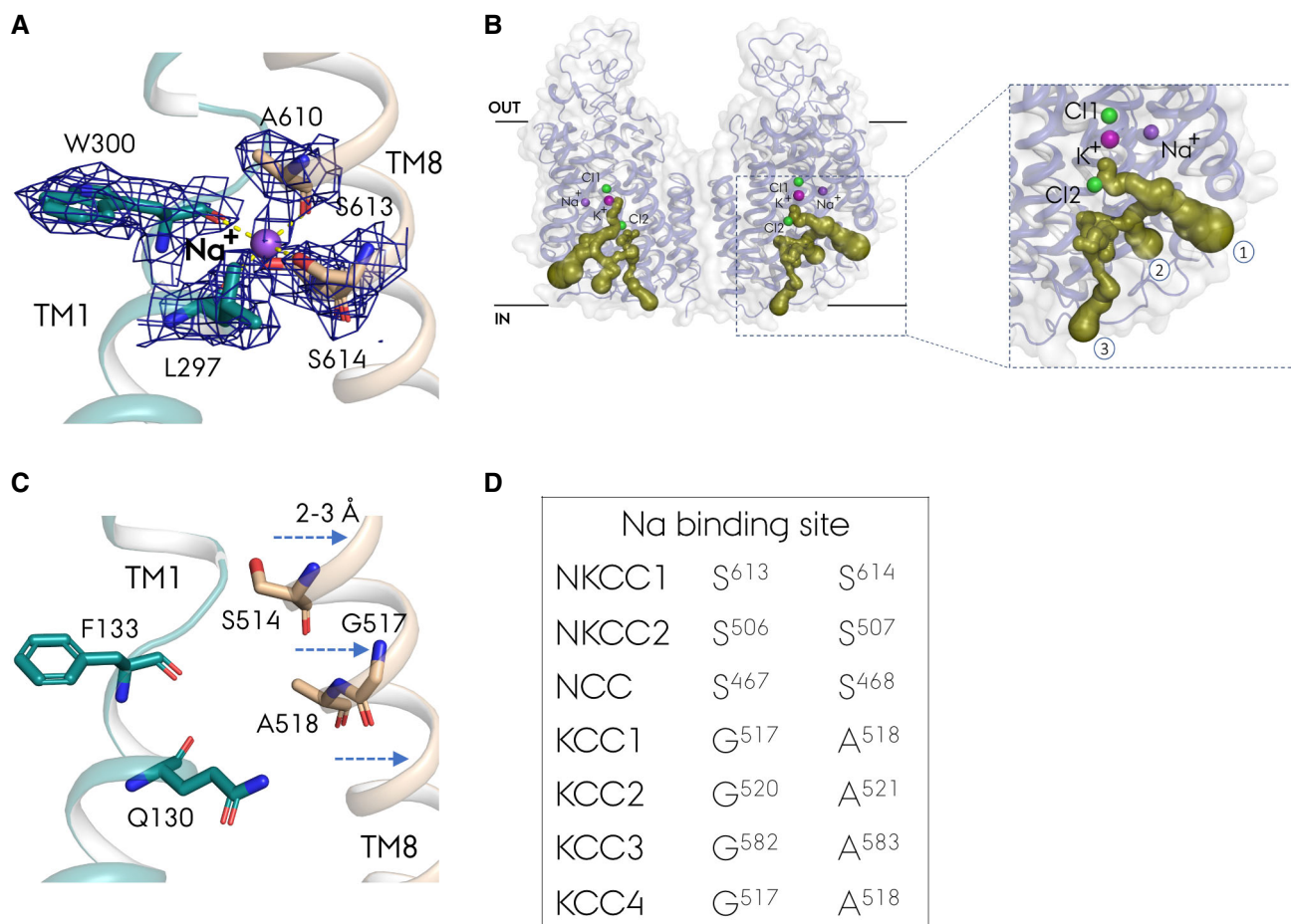


**Figure 2. Na<sup>+</sup>-binding site.**

- A The Na<sup>+</sup>-binding site in hNKCC1. The ion has a trigonal-bipyramidal coordination by five ligands. Scaffold helices are presented in wheat and bundle helices are presented in cyan; the Na<sup>+</sup> ion is presented as a purple sphere and coordinating residues are presented as sticks. The density of the Na<sup>+</sup> ion and residues important for Na<sup>+</sup> coordination is presented.
- B Three potential intracellular exit pathways predicted by MOLE 2.5. The Na<sup>+</sup> ion is presented as a purple sphere, the K<sup>+</sup> ion is presented as a magenta sphere, and the Cl<sup>-</sup> ions are presented as green spheres.
- C KCC1 does not bind Na<sup>+</sup> due to a G-A substitution on TM8. Additionally, the helix is moved 2–3 Å away when compared with hNKCC1 (KCC1 PDB code: 6KKR).
- D Sequence alignment of the Na<sup>+</sup> site of the CCC transporters. The G-A substitution of KCC1–4 on TM8 prevents Na<sup>+</sup> binding.

### Coupling network within the main substrate-binding pocket

The substrate site in hNKCC1 accommodates a K<sup>+</sup> and the Cl<sup>-</sup> ion at the Cl1 site. The K<sup>+</sup> ion is coordinated by the carbonyl oxygens of N298, I299, T499, and P496 and the hydroxyl groups of Y383 and T499 (Fig 4A). Y383 seems to have an important role in substrate specificity in NKCCs (Chew *et al*, 2019; Zhang *et al*, 2021) and KCCs (Liu *et al*, 2019; Reid *et al*, 2020; Xie *et al*, 2020; Chi *et al*, 2021a,b), whereas the same position in NCCs (not transporting K<sup>+</sup>) is a conserved histidine residue, which may substitute for K<sup>+</sup> (Fig 4B; Hartmann & Nothwang, 2014). Previous functional studies demonstrated that mutation of the tyrosine residue results in impairment of transport of the human NKCC1 (Somasekharan *et al*, 2012). The corresponding Y108<sup>LeuT</sup> and Y176<sup>SERT</sup> are crucial residues for substrate-induced conformational change from the outward-facing to the inward-facing states in SLC6 transporters and participate in an interaction network between the bundle (TM 6 and 7) and

scaffold domain (TM 3) in the extracellular pathway (Zhang *et al*, 2018; Fig 4B). In hNKCC1, this network involves Y383 on TM3 that coordinates the K<sup>+</sup> ion as well as T499 on the unwound part of TM6. Highlighting the importance of these residues, Tl<sup>+</sup> influx in mammalian cells expressing hNKCC1 Y383F and Y383S mutants was impaired when compared to wild-type hNKCC1 (Fig 4C and D), despite similar cell surface expression of the mutants and wild-type NKCC1 (Fig EV5C and D).

On the opposite side of the binding pocket, Y533 on the bundle domain of TM7 interacts with A497 on TM6 as well as the Cl<sup>-</sup> ion at the Cl1 site through a water-mediated interaction (Fig 4A). A similar substrate coordination network in SLC6 transporters has been investigated by mutations for the equivalent and conserved E290<sup>LeuT</sup> residue (or for other SLC6 transporters) inquiring the Na<sup>+</sup> site and chloride binding (Kantcheva *et al*, 2013; Penmatsa *et al*, 2013; Coleman *et al*, 2016; Zhang *et al*, 2018). Indeed, replacing Y533 in hNKCC1 with a phenylalanine or glutamate

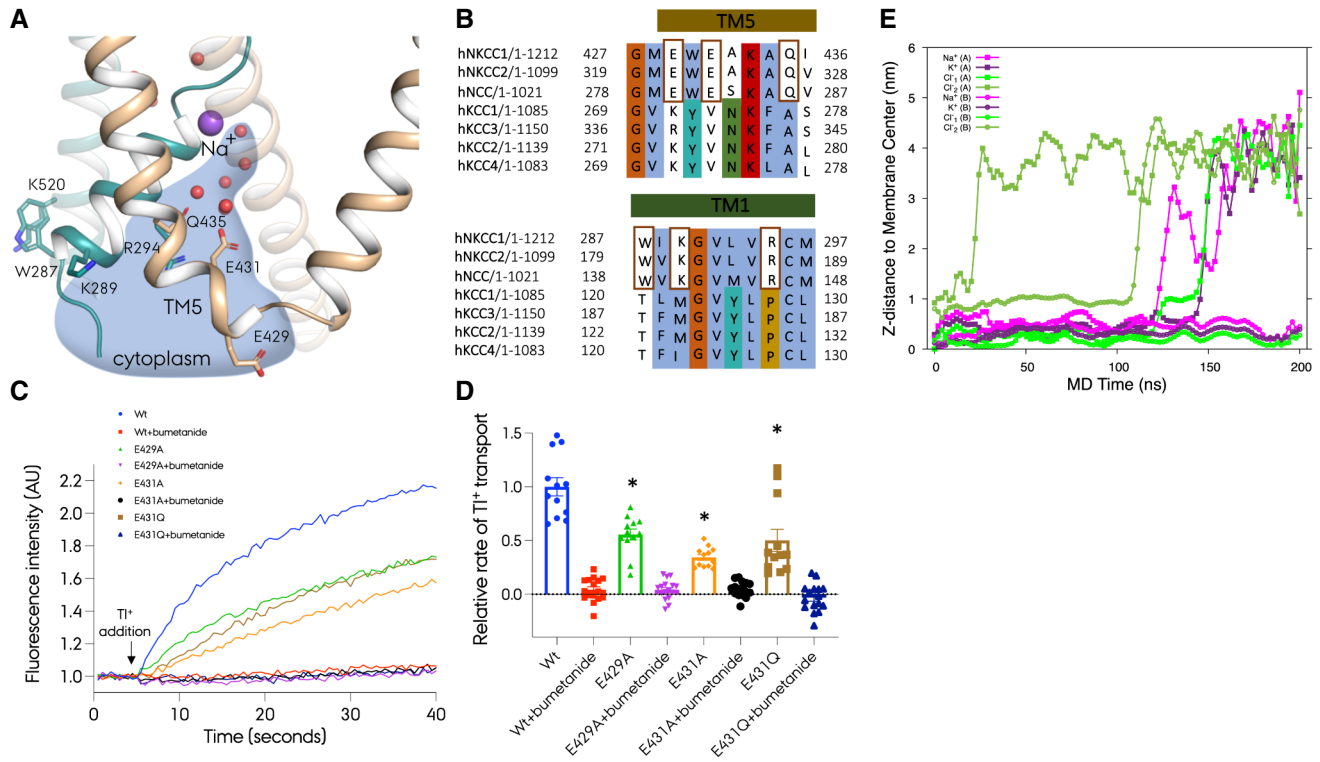


**Figure 3. Intracellular Na<sup>+</sup> release pathway.**

**A** The intracellular Na<sup>+</sup> release pathway of hNKCC1. The pathway is filled with water molecules (red spheres) and lined with two negatively charged glutamate residues (Glu429 and Glu431). Scaffold helices are presented in wheat and bundle helices are presented in cyan; the Na<sup>+</sup> ion is presented as a purple sphere.

**B** Sequence alignment of the intracellular part of TM5 and TM1a of CCC transporters. The Na<sup>+</sup>-dependent CCC transporters contain two conserved glutamate and a glutamine residue within TM5 and a positively charged lysine and arginine residues on TM1a.

**C** Substrate release order determined by MD simulations. The Cl<sup>-</sup> bound at Cl2 leaves first, then the Na<sup>+</sup> ion, followed by K<sup>+</sup> and Cl<sup>-</sup> from the main binding site.

**D, E** Transport kinetics and relative initial transport rates of wild-type hNKCC1 and NKCC1 with a mutation within the potential Na<sup>+</sup> release pathway (E429A, E431A, and E431Q) with and without addition of bumetanide; mean ± SEM, n = 3 independent experiments with 4–6 replicates for each time point per experiment. See Fig 1 legend for normalization approaches.

Source data are available online for this figure.

residue significantly reduced TI<sup>+</sup> influx in transfected mammalian cells (Fig 4C and D).

**Second Cl<sup>-</sup>-binding site (Cl2) is solvated**

Besides the Cl<sup>-</sup> ion bound at the main substrate site, NKCC1 transports a second Cl<sup>-</sup> ion accommodated at the Cl2-binding site located further toward the cytoplasmic interface. The second Cl<sup>-</sup> ion is coordinated by Y686 on TM10, and additionally it interacts with the unwound part of TM6 (Fig 5A). In contrast to the conservation of the Na<sup>2</sup>-binding site throughout most APC transporters, the two Cl<sup>-</sup> sites of hNKCC1 are not found in other APC transporter families. Interestingly, however, the Cl2 site of hNKCC1 superimposes with the carboxylate side-chain group of a strictly conserved glutamate residue on TM2 of SLC6 transporters (e.g., E136<sup>SERT</sup> and E62<sup>LeuT</sup>), which is important for substrate transport and conformational changes (Chen et al, 2001; Sucic et al, 2002; Sen et al, 2005; Korkhov et al, 2006; LeuT shown in Fig 5B). Replacement of Y686 with a serine or glutamate residue reduces transport activity of hNKCC1 to 25% indicating that the residue is central for coordination of the Cl<sup>-</sup> ion and coupled transport (Fig 5C and D). In

hNKCC1, the Cl<sup>-</sup> ion at Cl2 bridges an interaction between TM10 and TM6, whereas the conserved glutamate residue of SLC6 transporters connects TM2 with TM6 and interacts with another glutamate on TM10 (e.g., E508<sup>SERT</sup> and E419<sup>LeuT</sup>). An interaction between TM2 and TM10 is present in all CCC transporters—N690 in hNKCC1 of TM10 interacts with S337 and T334 of TM2 (Fig 5A and E). Importantly, and in contrast to the buried Na<sup>+</sup> ion, the Cl<sup>-</sup> ion bound at Cl2 interacts with cytoplasmic water molecules, which are clearly visible in the cryo-EM map (Fig 5A).

**Substrate release**

The well-defined structure with assigned ion-binding sites, lipids, sterols, and solvation of the Cl2 site prompted us to investigate the substrate-bound complex by MD simulations. We performed 20 independent all-atom MD simulations of the transmembrane domain of our dimeric hNKCC1 over 8 μs accumulated trajectories. In agreement with the observation of hydration of Cl<sup>-</sup> at the Cl2 site, the solvated Cl<sup>-</sup> ion was not stably bound and was able to leave its binding site for tens of ns and exchange for solvent Cl<sup>-</sup> ions. However, in contrast to the reversible exchange of Cl<sup>-</sup> at the Cl2 site, a

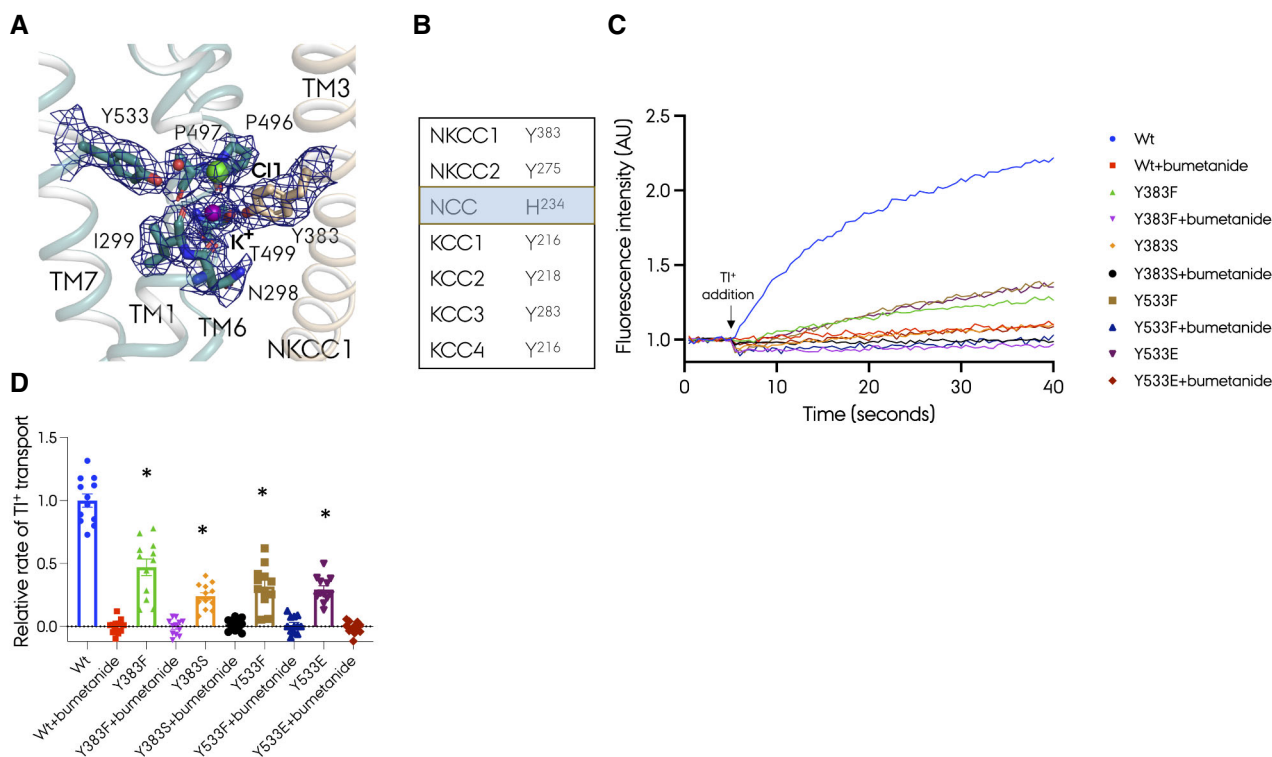


**Figure 4. Coordination network within the main binding pocket characterized for.**

- A** hNKCC1. The binding pocket accommodates a  $K^+$  and  $Cl^-$  ion coordinated by TM3 from the scaffold domain (wheat) and TM1, TM6, and TM7 from the bundle domain (cyan). The density of the ions and residues important for substrate coordination is presented. The  $K^+$  ion is presented as a magenta sphere, the  $Cl^-$  ion is presented as a green sphere, and a water molecule is presented as a red sphere.
- B** Sequence alignment of the crucial amino acid residue on TM3 of CCC transporters. In contrast to other members of the SLC12 family that contain a tyrosine residue coordinating the  $K^+$  ion at this position, hNCC contains a histidine residue that in its charged state could substitute the  $K^+$  ion.
- C, D** Transport kinetics and relative initial transport rates of wild-type hNKCC1 and NKCC1 with a mutation within the K- and Cl1-binding pocket (Y383F, Y383S, Y533F, and Y533E) with and without addition of bumetanide; mean  $\pm$  SEM,  $n = 3$  independent experiments with 4–6 replicates for each time point per experiment. See Fig 1 legend for normalization approaches.

Source data are available online for this figure.

subsequent release of the  $Na^+$  ion upon release of  $Cl^-$  ion from Cl2 marks a point of no return, and neither the  $Cl^-$  nor the  $Na^+$  ions will rebind to their respective sites thereafter (Fig 3C and Movie EV2). As also suggested by the structural analysis and mutational studies, E431 plays an important role in the MD simulations of  $Na^+$  release by transient interactions that escort the  $Na^+$  ion to the cytoplasmic environment. Additionally, in some of our simulations, we further observed that the  $K^+$  substrate and the  $Cl^-$  ion at Cl1 site left the binding sites at almost the same time after the release of  $Cl^-$  from Cl2 and  $Na^+$ , although complete substrate release events in the hNKCC1 dimer were rarely observed probably due to limited simulation time (200 ns for each; Fig 3C and Movie EV2). Our atomistic MD simulations support a substrate release order in which  $Cl^-$  at Cl2 site first releases and reversibly, then  $Na^+$  from a Cl2 released state, and lastly,  $Cl^-$  at the Cl1 site and  $K^+$  in a cooperative manner.

## Discussion

Here, we report a cryo-EM structure at an overall 2.6 Å resolution of the transmembrane domain of the human NKCC1 in a dimeric form with both protomers adopting an occluded, substrate-bound and

inward-oriented state. The  $Na^+$  ion of NKCC1 binds at the conserved  $Na^+$  site of APC transporters (often denoted the Na2 site), and the  $K^+$  and  $Cl^-$  ions (Cl1) bind at the general substrate-binding pocket of the APC superfamily. The second  $Cl^-$  ion (Cl2 site) is located closer to the cytoplasmic interface at a solvated pathway in contact with the cytoplasmic environment.

Our cryo-EM maps revealed the presence of interfacial lipids, which are also observed in the zNKCC1 structure (Chew *et al*, 2019). These interfacial lipid molecules appear to stabilize the dimeric state, which is only retained for hNKCC1 when solubilized and purified in mild detergents like lauryl maltose neopentyl glycol (LMNG) and glyco-diosgenin (GDN), whereas a monomeric state is obtained in n-dodecyl- $\beta$ -D-maltopyranoside (DDM). These findings are different from the KCC transporters that appear to be less lipid dependent and where DDM was routinely used for protein handling without disruption of the dimer (Liu *et al*, 2019; Chi *et al*, 2021b). This may be a result of the different oligomeric arrangements of the protomers in the transmembrane region of NKCC1 vs. KCC structures (Appendix Fig S2D). A recent study proposes that the dimer interface is separated by activation of NKCC1 and bumetanide inhibition (Zhao *et al*, 2022), which would potentially place an important function of the lipid structure at the dimer interface.

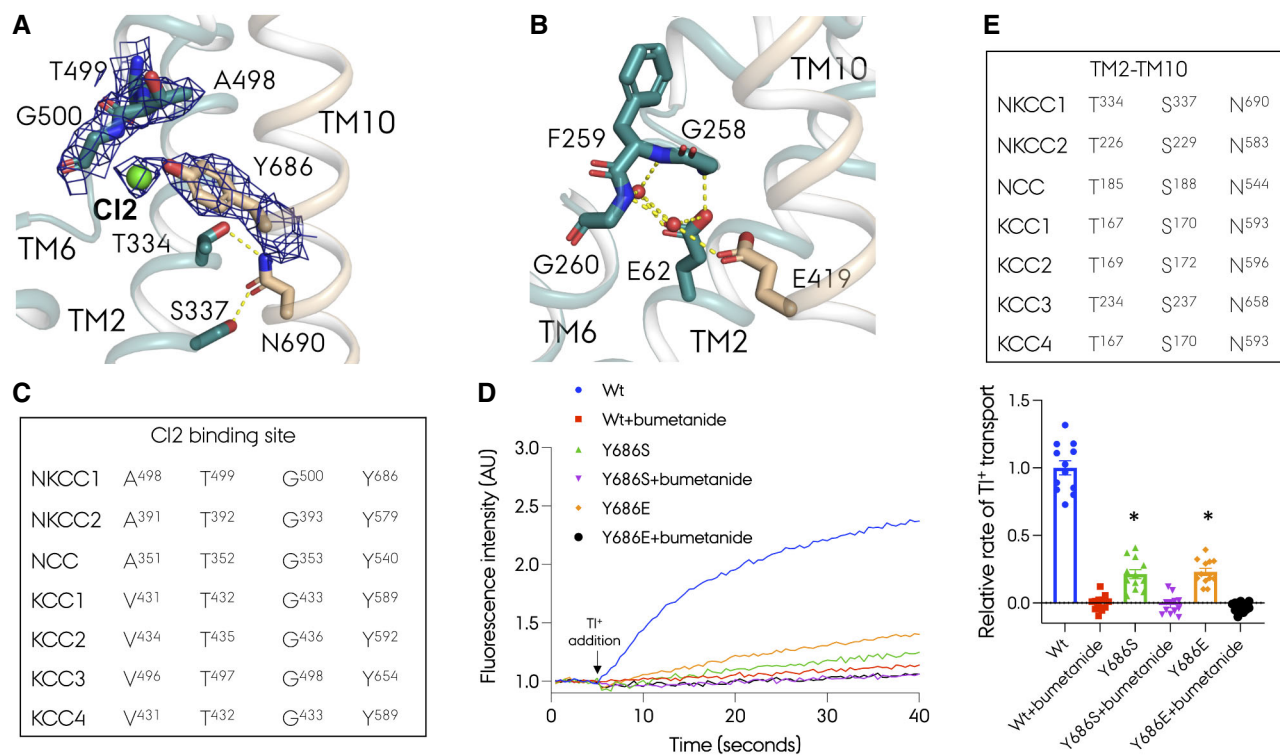


**Figure 5. Coordination network between TM2-TM10 and the unwound part of TM6 in.**

- A** Cl<sub>2</sub>-binding site with the density map. The Cl<sup>-</sup> ion is coordinated by the scaffold helix TM10 (wheat color) and the unwound part of TM6 belonging to the bundle domain (cyan color). The Cl<sup>-</sup> ion is presented as a green sphere.
- B** LeuT in complex with L-leucine and Na<sup>+</sup> (PDB code:2A65). Water molecules are presented as red spheres.
- C, D** Sequence alignment of residues linking TM2 and TM10 and residues within the Cl<sub>2</sub>-binding site.
- E** Transport kinetics and relative initial transport rates of wild-type hNKCC1 and NKCC1 with a mutation within the Cl<sub>2</sub> site (E429A, E431A, and E431Q) with and without addition of bumetanide; mean ± SEM, *n* = 3 independent experiments with 4–6 replicates for each time point per experiment. See Fig 1 legend for normalization approaches.

Source data are available online for this figure.

In addition to interfacial lipids, our cryo-EM map revealed three cholesterol molecules per protomer (represented by cholesterol hemisuccinate, CHS), all localized toward the extracellular side of the membrane and stabilizing the inward-facing conformation of NKCC1. Comparing NKCC1 and Na<sup>+</sup> independent KCC structures, cholesterol sites are generally associated with inward-oriented states, i.e., the substrate-releasing state of NKCC1 and the substrate-loading state of KCC transporters. Interestingly, both NKCC1 and KCC2 have been shown to associate with cholesterol-rich lipid rafts in the plasma membrane, and cholesterol could regulate their transport cycle (Hartmann *et al*, 2009). Mutation of central phenylalanine or tyrosine residues involved in  $\pi$ - $\pi$  interactions at the cholesterol sites of NKCC1 resulted in reduced transport activity, suggesting that cholesterol binding is important for the transport activity of NKCC1. We also analyzed the sites by MD simulations, and find that the modeled sites 1 and 2 are stable. An F487A mutation at CHS site 1 destabilized cholesterol binding, however, not enough to dissociate cholesterol within the time range of simulations. Using M $\beta$ CD, the effect of cholesterol extraction from the cell membrane was studied. At low M $\beta$ CD concentrations, there was increased NKCC1 activity, but inhibition of NKCC1 activity was

observed at higher extraction levels before the cytotoxic effects of M $\beta$ CD were observed at the highest extraction levels. M $\beta$ CD can cause plasma membrane accumulation of the cotransporters NKCC2 and NCC (Ares & Ortiz, 2010; Rosenbaek *et al*, 2014). Hence, the direct effects of cholesterol depletion on NKCC1 activity are most likely of complex nature, where both dynamic function and stability of the transporter are directly affected by cholesterol levels, and secondary effects play an increasingly important role in more complete depletion of cholesterol.

Interestingly, a regulatory role of cholesterol was found also for human SERT and dDAT (Penmatsa *et al*, 2013; Coleman *et al*, 2016). Here, cholesterol was found to stabilize outward-facing conformations, and cholesterol depletion shifted the conformation toward an inward-facing conformation of the serotonin transporter and changed the substrate affinity, turnover rate, and maximum transport velocity (Laursen *et al*, 2018).

The Na<sup>+</sup>-binding site of NKCC1 is highly conserved throughout Na<sup>+</sup>-dependent APC transporters (Appendix Fig S3A–C; Yamashita *et al*, 2005; Faham *et al*, 2008; Weyand *et al*, 2008; Krishnamurthy *et al*, 2009; Khafizov *et al*, 2012; Perez *et al*, 2012; Penmatsa *et al*, 2013; Malinauskaite *et al*, 2014). A crucial role of an equivalent site



is also retained in many Na<sup>+</sup> independent transporters (exchangers), also adopting the LeuT fold (Appendix Figs S3D–F and S4), often with a positively charged side chain at this location undertaking the role of the Na<sup>+</sup> site and creating a link between TM1 and TM8 (e.g., R262 of CaiT (Kalayil *et al*, 2013), K158 in ApcT (Shaffer *et al*, 2009), and K154 in BasC (Errasti-Murugarren *et al*, 2019)). However, a comparison of NKCC1 and the Na<sup>+</sup> independent KCC transporters reveals that the latter does not contain any basic residues substituting for Na<sup>+</sup> near the Na2 site, thereby suggesting a different mechanism compared to other Na<sup>+</sup>-independent APC transporters (Fig 2C and Appendix Fig S5). Indeed, KCC transporters perform a unidirectional outward transport of K<sup>+</sup> and Cl<sup>-</sup> ion from the cytoplasm to the extracellular space, and outward transport is Na<sup>+</sup> independent for all LeuT-fold transporters.

Our structure of hNKCC1 allowed us to also consider a homology model for the transmembrane domain of the Na<sup>+</sup>/Cl<sup>-</sup> transporting human NCC and the ion-coupling mechanisms and binding site specificity for this K<sup>+</sup> independent transporter. As expected, the Na<sup>+</sup>-binding site in NCC is fully conserved compared to NKCC1 (Fig 2D). NCC contains a histidine residue (H234<sup>NCC</sup>) instead of the crucial tyrosine on TM3 of NKCC and KCC that coordinates the K<sup>+</sup> ion (Fig 4B; Hartmann & Nothwang, 2014), and in its protonated, positively charged state, the histidine residue could act in lieu of a K<sup>+</sup> ion. Moreover, the central localization on TM3 would allow the histidine residue still to participate in the important coordination network within the main binding pocket and maintain the high substrate selectivity and coupling that otherwise involves K<sup>+</sup> for NKCC and KCC transporters. Surprisingly, the NCC homology model also reveals that both Cl<sup>-</sup> sites are conserved, even though NCC only translocates one Cl<sup>-</sup> ion (Fig 5C).

Earlier studies of NKCC1 provided evidence that the two Cl<sup>-</sup>-binding sites are non-equivalent and exhibit different Cl<sup>-</sup> affinities with a low Cl<sup>-</sup> affinity site identified closer to the cytoplasm and in near proximity to the Na<sup>+</sup> site ( $K_m = 55.3$  mM, corresponding to the Cl2 site in our structure) and a high Cl<sup>-</sup> affinity site found closer to the extracellular environment and in close proximity to the K<sup>+</sup> site ( $K_m = 5.1$  mM, corresponding to the Cl1 site in our structure). In addition to the significant difference in Cl<sup>-</sup> affinity between the two sites, the binding characteristics of the two sites are very different, as Cl2 only was able to bind and transport Cl<sup>-</sup> ions, whereas Cl1 could also bind and transport NO<sub>3</sub><sup>-</sup> and SCN<sup>-</sup> (Brown & Murer, 1985; Kinne *et al*, 1986; Turner & George, 1988; Russell, 2000). We speculate that if the two predicted Cl<sup>-</sup> sites in NCC exhibit similar properties as NKCC1, one of the sites might act as a substrate site, whereas the second site with lower Cl<sup>-</sup> affinity could function as an auto-inhibitory site that blocks NCC activity when the cytoplasmic Cl<sup>-</sup> concentration is high, independent of the Na<sup>+</sup> gradient. Indeed, high intracellular Cl<sup>-</sup> concentration is inhibitory for NCC, although it is proposed to be indirect via inhibition of the WNK/SPAK kinase pathway (Hoorn *et al*, 2020).

The conserved Cl<sup>-</sup> sites in NKCC1 and NCC are also described for KCC transporters, with published KCC structures having both Cl<sup>-</sup> sites occupied despite only transporting one Cl<sup>-</sup> ion (Liu *et al*, 2019). Mutation of either Cl<sup>-</sup> site impairs transport, suggesting that both are required for KCC transporter function (Liu *et al*, 2019). Structure superposition of hNKCC1 and hKCC1 reveals a slight 2–3 Å displacement of TM8 in KCC due to a lack of Na<sup>+</sup> binding that might impact Cl<sup>-</sup> transport at the Cl2 site

(Appendix Fig S5; Liu *et al*, 2019). Interestingly, the KCC transporters contain a flexible hydrogen bond network linking TM1 and TM8 that is absent in the Na<sup>+</sup>-dependent CCCs. L297<sup>hNKCC1</sup> is substituted with Q130<sup>hKCC1</sup> on TM1, and L616<sup>hNKCC1</sup> is substituted with Q521<sup>hKCC1</sup> on TM8. Both glutamine residues introduced in hKCC1 interact with an asparagine residue (N131<sup>hKCC1</sup>) and connect interactions between K<sup>+</sup>/Cl<sup>-</sup> transport sites and the Cl2 site, potentially playing a particular regulatory role in KCC transporters for Cl2 site coupling. We speculate that the Cl2 site is adapted for a specific Cl<sup>-</sup> sensory function in KCC transporters that activates Cl<sup>-</sup> efflux at high cytoplasmic concentrations of Cl<sup>-</sup> and oppositely blocks efflux at low cytoplasmic Cl<sup>-</sup> concentrations, besides being coupled to the K<sup>+</sup> gradient.

Interestingly, the Cl2 site in SLC12 transporters overlaps with completely conserved glutamate of TM2 in SLC6 transporters, e.g., E62<sup>LeuT</sup>, E66<sup>MhsT</sup>, and Glu136<sup>SERT</sup> (Fig 5B). The interaction of this glutamate residue and the unwound junction of TM6 is maintained throughout all the known states of SLC6 transporters, highlighting the importance of this interaction (Focht *et al*, 2021). For hNKCC1 (and SLC12 transporters in general), it seems that the Cl<sup>-</sup> ion together with Y686<sup>hNKCC1</sup> replaces the role of the conserved glutamate in SLC6 transporters and allows for transport translocation. The coordination network among TM2-TM10-Cl2-TM6 in NKCC1, therefore, appears to play the same role as the TM10-TM2–water–TM6 network within SLC6 transporters connecting the main binding site to distal rearrangements of the transporter.

Our cryo-EM structure of hNKCC1 also shows solvation of the Cl<sup>-</sup> ion bound at the Cl2 site, but not of the Na<sup>+</sup> ion. This is different from the SLC6 transporters, where the Na<sup>+</sup> ion (here denoted a Na2 site) is the first solvated substrate and also released first to the intracellular environment followed by the remaining substrates (Malinauskaitė *et al*, 2014; Li *et al*, 2019). Our MD simulations of NKCC1 reveal that in agreement with the observed solvation, the Cl<sup>-</sup> ion at Cl2 is the first substrate to be released. However, this is reversible and its release is not a determining step in the transport mechanism. The reversible exchange with the cytoplasmic environment is also consistent with the regulatory role of this site as proposed above for NCC and KCCs. First, when the Na<sup>+</sup> ion leaves as the second event in NKCC1 dynamics, none of the released ions rebind, and later the K<sup>+</sup> and Cl<sup>-</sup> ions at the main substrate cavity leave and the transporter can return to the outward-open conformation (Fig 3C). Lipid and cholesterol sites may play an important role in these transitions, as discussed above. Our MD simulations also confirm that the Na<sup>+</sup> ion is released through a pathway along TM5 extending from the binding site to the cytoplasm (pathway 1 in Fig 2B). Two negatively charged glutamate residues (E429 and E431) conserved within the Na<sup>+</sup>-dependent CCCs guide the Na<sup>+</sup> ion from its binding site and to the cytoplasm. Our mutational studies of these residues are consistent with an important role in transport activity. Bacterial SLC6 transporters contain a conserved glutamate residue at a similar position to E429, e.g., E192<sup>LeuT</sup>, which too has been proposed to guide Na<sup>+</sup> to the cytoplasm (Shaikh & Tajkhorshid, 2010). This residue corresponds as well to the conserved D182 in vSGLT (SLC5), which also has been implicated in facilitating Na<sup>+</sup> diffusion (Li & Tajkhorshid, 2009).

There is currently no consensus on the potential substrate release mechanism of CCC transporters. Two different substrate binding and release models were proposed previously (Lytle *et al*, 1998;

Delpire & Gagnon, 2011). In the so-called “glide-symmetry” model, the outward-facing conformation of NKCC1 first binds the Na<sup>+</sup> ion, then the Cl<sup>-</sup> at the Cl2 site, followed by K<sup>+</sup> and Cl<sup>-</sup> from the Cl1 site. Then, in the inward-facing state, the substrates are released in the same order, e.g., with Na<sup>+</sup> first and then Cl<sup>-</sup> from the Cl2 site (Lytle *et al*, 1998). The “steady state” model, on the other hand, suggests that the outward-open state first binds Cl<sup>-</sup> at the Cl2 site, then the Na<sup>+</sup> ion, followed by the second Cl<sup>-</sup> ion at the Cl1 site and K<sup>+</sup>, whereas the substrates are released in reverse order to the cytoplasmic environment (Delpire & Gagnon, 2011). The substrate release mechanism proposed in our work does not fit either of the two earlier models for substrate release, but it would be closer to the glide-symmetry model, although with release first from the Cl2 site and then Na<sup>+</sup>.

In summary, SLC12 transporters are of great importance for the proper functioning of organisms ranging from humans and vertebrate animals through plants (Colmenero-Flores *et al*, 2007) and fungi to insects, worms, and cyanobacteria (Hartmann *et al*, 2014). Insight into their three-dimensional structure and mechanistic details of substrate binding, translocation, and release might lead to a better understanding of the role of these transporters in normal physiology and their pathophysiological roles. Our 2.6 Å cryo-EM structure of the occluded and inward-facing hNKCC1 provides not only a direct insight into substrate accommodation but also resolves the intracellular water networks and reveals, solvation of Cl<sup>-</sup> at Cl2, but not of Na<sup>+</sup> (Figs 2A and 5A). Insight into the ion coupling networks, regulation, and the transport mechanism of the SLC12 transporters gained from this work on hNKCC1 can improve our understanding of their physiological roles and regulation and guide further investigations of their structure, function, and mechanism.

## Materials and Methods

### Reagents

All chemicals were obtained from Sigma unless stated otherwise.

### Expression and purification of the human NKCC1

The full-length human NKCC1 with an N-terminal 8xHis-TwinStrep-GFP-tag-3Cprotease\_cleavage\_site was expressed in HEK293 GnT1<sup>-</sup> (ATCC) cells by use of the BacMam system as described earlier (Goehring *et al*, 2014). HEK293 GnT1<sup>-</sup> cells were grown to a density of  $3 \times 10^6$  cells/ml at 37°C and 5% CO<sub>2</sub> on an orbital shaker at 120 rpm. The cells were then transduced with the P3 NKCC1 BacMam virus to an MOI of three and the cells were further incubated in the incubator. Twenty-four hours post-transduction, 10 mM sodium butyrate was added to the cells and the temperature was lowered to 30°C with 5% CO<sub>2</sub> while shaking (120 rpm). After 48 h, the cells were harvested by centrifugation at 6,200 g at 4°C. The cell pellets were stored at -80°C.

The frozen cell pellet was thawed and resuspended in a buffer composed of 200 mM NaCl, 200 mM KCl, 20 mM Tris-HCl, pH 8.0, 10% (v/v) glycerol, and 0.07 mM bumetanide\*. The cells were lysed by sonication and centrifuged for 20 min at 20,000 x g at 4°C. The collected supernatant was further centrifuged at 163,000 x g for 3 h at 4°C and the pellet was thereafter resuspended in the same

buffer with a ratio of 10 ml buffer per 1 g of wet pellet. One percent lauryl maltose neopentyl glycol (LMNG, Anatrace) and 0.1% cholesteryl hemisuccinate (CHS, Anatrace) were added and the membrane proteins were solubilized overnight at 4°C. The mixture was then centrifuged at 14,000 g for 30 min, the insoluble fraction was discarded, and the supernatant was incubated with Strep-Tactin resin for 3 h. The resin was washed with 10 column volumes washing buffer containing 0.01% LMNG, 0.001% CHS, 200 mM NaCl, 200 mM KCl, 20 mM Tris-HCl pH 8.0, 10% (v/v) glycerol, and 0.07 mM bumetanide. The hNKCC1 protein was eluted with a wash buffer supplemented with 5 mM desthiobiotin. The sample was then cleaved overnight with 3C protease and concentrated at 3 mg/ml. The protein was further purified by gel filtration (Superose 6 3.2/300) on an Äkta Purifier system equilibrated in a buffer composed of 0.01% glycol-diosgenin (GDN, Anatrace), 200 mM NaCl, 200 mM KCl, 20 mM Tris-HCl, pH 8.0, and 0.07 mM bumetanide. Peak fractions were collected and concentrated to 0.9–1.5 mg/ml for cryo-EM studies.

### Thallium-ion (Tl<sup>+</sup>) flux transport assay

The NKCC1 mutant constructs were designed in the same way as the wt NKCC1 construct used for structure determination. The mutants were prepared by GenScript. Activity levels of the wild-type NKCC1 transporter and NKCC1 mutants were determined by use of the thallium-ion flux transport assay. The construct with an N-terminal 8xHis-TwinStrep-GFP-tag was expressed in GripTite HEK293 MSR cells (Thermo Fisher) in black 96-well plates with transparent bottoms. The cells were maintained in DMEM GlutaMAX medium (Gibco) with the addition of 10% FBS and 1× non-essential amino acid (NEAA) cell culture supplement. A total of 50,000 cells were seeded out per well and the cells were incubated for 24 h at 37° with 8% CO<sub>2</sub>. On the day of transfection, 3 µl Lipofectamine 3000 (Invitrogen) was mixed with 47 µl Opti-Mem medium (Gibco). Separately, 1 µg DNA was diluted in 36 µl Opti-MEM medium with the addition of 4 µl P3000 reagent (Invitrogen), and thereafter, the Lipofectamine 3000 solution was mixed with the DNA solution. After 15 min of incubation, 10 µl of the mixture was added to each of the wells. After 5–6 h, 100 µl DMEM medium, 1× NEAA, and 30% FBS were added to each well. The activity assay was performed 72 h post-transfection of the cells.

On the day of the experiment, the DMEM medium was exchanged for 80 µl loading buffer containing probenecid, PowerLoad, and FluxOR II Reagent from the FluxOR II Red Potassium Ion Channel Assay kit (Thermo Fisher Scientific) and a low Cl<sup>-</sup> buffer (15 mM Na-HEPES, pH 7.4, 135 mM Na-gluconate, 1 mM MgCl<sub>2</sub>·6H<sub>2</sub>O, 1 mM Na<sub>2</sub>SO<sub>4</sub>, and 1 mM CaCl<sub>2</sub>·2H<sub>2</sub>O). The cells were incubated with the loading buffer for 1 h at room temperature, and thereafter, they were washed once with the low Cl<sup>-</sup> buffer with the addition of probenecid, followed by the addition of 80 µl buffer to each well.

The assay was performed using the ENSPIRE 2300 kinetic dispense microplate reader (PerkinElmer). First, GFP fluorescence was measured for later normalization (excitation at 480 nm, emission at 510 nm, 100 flashes, 3 repeats, and 0.1 s). After 5 s of baseline recording (10 repeats), the transport assay was initiated by the addition of 20 µl stimulation buffer containing low Cl<sup>-</sup> buffer, 135 mM NaCl, and 5 mM thallium sulfate with or without 165 µM

bumetanide (final concentrations of 27 mM NaCl, 1 mM thallium sulfate, and 33  $\mu$ M of bumetanide). The excitation wavelength was set to 565 nm and the emission wavelength was set to 583 nm. The plate was read every 0.5 s for 80 repeats (40s).

The thallium-ion flux assay for constructs containing mutations within the cholesterol-binding sites was performed using the FluxOR II Green Potassium Ion Channel Assay kit (Thermo Fisher Scientific). The assay was performed in the same way as described above; however, in the final thallium uptake measurements, the excitation wavelength was set to 490 nm and the emission wavelength was set to 523 nm.

For cholesterol depletion using methyl- $\beta$ -cyclodextrin (M $\beta$ CD, #C4555, Sigma), transfected cells were grown on 96-well plates, and media were replaced with PBS-CM (PBS pH 7.5 with the addition of 1 mM CaCl<sub>2</sub> and 0.1 mM MgCl<sub>2</sub>) before measurement of GFP intensity. Cells were then pre-incubated in DMEM medium for 2 h at 37°C, followed by 30 min incubation with different M $\beta$ CD concentrations (0–15 mM) dissolved in DMEM media at 37°C. The media were removed and replaced with loading buffer containing M $\beta$ CD (same concentrations as pre-incubation) and the cells were incubated at RT for 1 h before performing the thallium uptake assay as described. Cell viability was assessed using similar M $\beta$ CD concentrations in non-transfected cells. A similar approach for the thallium uptake assay was followed, however, the FluxOR II reagent was removed from the loading buffer. After 1 h incubation at RT, the loading buffer was replaced with the redox-sensitive dye resazurin (R&D systems, #AR002) diluted 1:10 in DMEM medium, and cells were incubated at 37°C for 1 h. The reduction of the non-fluorescent resazurin to the highly fluorescent resorufin in viable cells was measured with an excitation wavelength of 544 nm and emission wavelength of 590 nm. A reduction in fluorescence is an indicator of reduced cell viability. Data were obtained from three independent experiments with 4–6 replicates for each time point per experiment.

### Biotinylation assay

Cell surface protein biotinylation was performed to estimate the plasma membrane expression of various NKCC1 mutants relative to the wild-type transporter. The N-terminal 8xHis-TwinStrep-GFP-tagged NKCC1 constructs were expressed in GripTite HEK293 MSR cells (Thermo Fisher) in 24-well plates. The transfection of cells was performed in the same way as done for the Tl<sup>+</sup> uptake assay, but the amounts were scaled up. The biotinylation assay was performed 72 h after transfection of the cells.

The cells were washed in basic buffer (135 mM NaCl, 5 mM KCl, 1 mM CaCl<sub>2</sub>·2H<sub>2</sub>O, 1 mM MgCl<sub>2</sub>·6H<sub>2</sub>O, 1 mM Na<sub>2</sub>HPO<sub>4</sub>·2H<sub>2</sub>O, 1 mM Na<sub>2</sub>SO<sub>4</sub>, and 15 mM Sodium HEPES, pH 7.4) and incubated in the low Cl<sup>-</sup> buffer (same as in uptake assay) for 1 h at 18–24°C. Thereafter, the cells were placed on ice and washed with ice-cold PBS-CM buffer (PBS pH 7.5 with the addition of 1 mM CaCl<sub>2</sub> and 0.1 mM MgCl<sub>2</sub>), followed by the biotinylation buffer (10 mM triethanolamine, 2 mM CaCl<sub>2</sub> and 125 mM NaCl). The cells were incubated in the biotinylation buffer with the addition of 1 mg/ml of sulfosuccinimidyl 2-(biotin-amido)-ethyl-1,3-dithiopropionate (EZ-link Sulfo-NHS-SS-biotin, Pierce) for 30 min at 4°C. After the incubation period, the cells were washed with ice-cold quenching buffer (50 mM Tris-HCl in PBS-CM buffer), followed by the PBS-CM

buffer. The cells were incubated in lysis buffer (20 mM Tris-HCl pH 8.0, 5 mM EDTA, 150 mM NaCl, 1% Triton X-100, 0.2% BSA, and Halt® protease inhibitors) for 30 min on ice, followed by probe sonication. Thereafter, the homogenates were centrifuged at 10,000 g for 5 min at 4°C. One fraction were retained for total NKCC1 protein abundance estimation and the remainder were incubated for 1 h with Neutravidin resin at room temperature under rotation. The resin was washed four times with PBS containing protease inhibitors and the bound protein was eluted by the addition of SDS-PAGE sample buffer to the resin. Western blotting was performed using standard methods using an anti-NKCC1 antibody.

### Cryo-EM sample preparation and data collection

For the preparation of grids, freshly purified hNKCC1 protein was used. Grids used were UltrAuFoil 1.2/1.3-300, glow discharged in residual atmospheric air for 45 s at 15 mA in a GloQube (Quorum). A 3  $\mu$ l drop was applied to the gold foil side of the grid and blotted in a Vitrobot Mark IV (ThermoFisher Scientific) using a blot force of 0 and blot time of 3–4 s before plunge freezing into liquid ethane cooled by liquid nitrogen. Micrograph data were collected on a Titan Krios G3i microscope (ThermoFisher Scientific) operated at 300 KeV equipped with a BioQuantum energy filter (energy slit width 20 eV) and K3 camera (Gatan). For data sets 1 and 2 (collected at the Krios2 microscope, EMBION facility, Aarhus University), a nominal magnification of 165,000 $\times$  was used, resulting in a physical pixel size of 0.507  $\text{\AA}^2/\text{px}$  with a total dose of 40.12 e<sup>-</sup>/ $\text{\AA}^2$  for data set 1 and a total dose of 39.78 e<sup>-</sup>/ $\text{\AA}^2$  for data set 2. For both data sets, movies were fractionated into 43 frames. The defocus range was set to 0.6–1.6 microns. For data set 3 (collected on Titan Krios at eBIC, Oxford, UK), a nominal magnification of 130,000 $\times$  was used, resulting in a physical pixel size of 0.83  $\text{\AA}^2/\text{px}$ , with movies saved in super-resolution pixel size of 0.415  $\text{\AA}^2/\text{px}$ . A total dose of 60.438 e<sup>-</sup>/ $\text{\AA}^2$  per movie was spread across 40 frames. The defocus range was set to 0.5–2.4 microns.

### Cryo-EM data processing

Data sets 1 and 2 were processed exclusively in RELION-3.1 (Scheres, 2012; Figs EV1 and EV2), whereas data set 3 was processed primarily in RELION-3.1 with some classifications performed using the heterogeneous refinement in Cryosparc3 (Punjani et al, 2017; Fig EV3). For all data sets, movies were motion corrected using RELION's own MotionCorr implementation and CTFFind4 (Rohou & Grigorieff, 2015) used for the determination of CTF parameters. Only micrographs with CTF fit resolution better than 4  $\text{\AA}$  were used further. Initial particle picking was done using RELION's LoG-picker on a small, random subset of micrographs in data set 1. Picked particles were extracted with a 512-pixel box, downsampled to 128 pixels, and subjected to 2D classification. Clear junk particles were discarded, and the remainder of the particles were used in 3D auto-refinement with the zNKCC1 reconstruction (EMD-0473) as an initial reference, lowpass filtered to 30  $\text{\AA}$  resolution. The resulting 3D reconstruction was used in 2D classification without image alignment, and the best 2D class averages were used for template-based particle picking on all micrographs for all three data sets. Particle images were extracted in a 480-pixel box, downsampled to 128 pixels, 2D classified using fast subsets, and skipping

CTF until the first peak. Clear junk classes were discarded, and the remainder raw particle set was subjected to 3D classification using fast subsets and 8 classes for data set 1 and 10 classes for data set 2. Particles from the 3D classes displaying features of an intact detergent micelle were selected and run through 3D auto-refinement followed by 2D classification without image alignment. Again, clear junk was discarded, and the remaining particles were re-extracted with downsampling to a 240-pixel box ( $1.014 \text{ \AA}^2/\text{px}$ ). Particles were again subjected to 3D classification now without fast subsets, using 8 and 6 classes for data sets 1 and 2, respectively. The 3D classes displaying clear density features of transmembrane helices were selected and subjected to unmasked 3D auto-refinement. The resulting consensus reconstructions were deemed of good enough quality to proceed with Bayesian polishing, followed by 3D auto-refinement with a mask around the transmembrane domains and application of C2 symmetry. The resulting masked 3D reconstructions were resolved better than  $3 \text{ \AA}$ , which upon merging of the particles from data sets 1 and 2 were 3D auto-refined to a high-quality reconstruction of  $2.6 \text{ \AA}$  resolution. For data set 3, subsequent to 2D classification and the first 3D classification in RELION-3.1, the particle image stack was further cleaned by discarding junk classes from a 2D classification job without image alignment. The resulting stack of 595,171 particle images was re-extracted in a 384-pixel box without downsampling before loaded into Cryosparc3 and further classified by *ab initio* reconstruction and heterogenous refinement using three classes. A single class of particles showed high-resolution features for the transmembrane helices, with the cytoplasmic domains being almost impossible to see. This new stack of particle images was taken back into RELION-3.1, cleaned yet again using 2D classification without image alignment, and the particle image was re-extracted in a 294-pixel box with downsampling to 240 pixels ( $1.016 \text{ \AA}^2/\text{px}$ ). The now clean stack of particle images was subjected to 3D auto-refinement, Bayesian polishing, and 3D auto-refinement again using a mask around the transmembrane domains and applying C2 symmetry. The resulting reconstruction showed high-quality density features resolved slightly better than  $3 \text{ \AA}$ . Using CTF refinement for anisotropic magnification to account for the small discrepancy in pixel size, the data set 3 particles were merged with the already combined particle data from data sets 1 and 2, to give a final 3D-refined reconstruction of  $2.55 \text{ \AA}$  average resolution for the transmembrane domains. Local resolution estimation was done using RELION's own implementation (Fig EV4).

### Model building and refinement

The transmembrane domain of hNKCC1 was built in Coot (Emsley *et al.*, 2010), guided by the *Danio rerio* NKCC1 structure (PDB entry: 6NPL; Chew *et al.*, 2019). The refinement was done by use of Real Space Refinement in Phenix (Afonine *et al.*, 2018) and manual corrections of the structure were performed in Coot. Validation of the structure was done in MolProbity (Williams *et al.*, 2018).

### System setup for molecular dynamics simulations

A model of hNKCC1 was constructed using the Cryo-EM structure of the transmembrane domain of hNKCC1 in a complex with its substrates, one  $\text{Na}^+$ , one  $\text{K}^+$ , and two  $\text{Cl}^-$  ions. In addition, four CHS molecules identified in the Cryo-EM structure were replaced by the

cholesterol molecules. The model was subsequently embedded into a flat, mixed lipid bilayer consisting of POPC/POPE/cholesterol at a 2:2:1 ratio, and solvated in a cubic water box containing  $0.1 \text{ M NaCl}$  and  $0.1 \text{ M KCl}$ . The size of the box was 13.1, 13.1, and 10.2 nm in the x, y, and z dimension, respectively, resulting in  $\sim 180,000$  atoms in total. The CHARMM36m force field was used for the protein and the CHARMM36 lipid force field was used for all lipid molecules.

In the MD simulations, the temperature was kept constant at 310 K using a Nose–Hoover thermostat with a 1 ps coupling constant, and the pressure at 1.0 bar using the Parrinello–Rahman barostat with a 5 ps time coupling constant. A cut-off of 1.2 nm was applied for the van der Waals interactions using a switch function starting at 1.0 nm. The cut-off for the short-range electrostatic interactions was also at 1.2 nm and the long-range electrostatic interactions were calculated by means of the particle mesh Ewald decomposition algorithm with a 0.12 nm mesh spacing. A reciprocal grid of  $112 \times 112 \times 96$  cells was used with fourth-order B-spline interpolation. All MD simulations were performed using Gromacs2019.6 (Abraham *et al.*, 2015). Twenty independent simulations (200 ns for each) were performed for the hNKCC1 model, thus resulting in 8  $\mu\text{s}$  simulations (20 runs  $\times$  200 ns  $\times$  2 monomers) in total.

## Data availability

The three-dimensional cryo-EM maps have been deposited into the Electron Microscopy Data Bank under accession number [EMD-14709](#). The atomic coordinates are deposited into the Protein Data Bank with accession number [7ZGO](#).

**Expanded View** for this article is available online.

## Acknowledgments

The authors are grateful for technical assistance to Tina Drejer, Tetyana Klymchuk, Anna Marie Nielsen, Bente Andersen and Anne Lillevang. We want to thank Thomas Boesen, Andreas Bøggild, and Taner Drace from the cryo-EM facility at Aarhus University for assistance with grid screening and numerous overnight data collections. We are thankful to Milena Timcenko, Jeppe Achton Nielsen, Søren Kirk Amstrup, and Jonathan Juhl for help with data processing and fruitful discussions about cryo-EM. We want to acknowledge Qi Wu for performing MS on the purified hNKCC1 sample in order to assure that sample of the expressed and purified hNKCC1 construct was correct. We acknowledge Diamond Light Source for access and support of the cryo-EM facilities at the UK's National Electron Bio-Imaging Centre (eBIC) under proposal AP27 (BI21404) funded by the Wellcome Trust, MRC, and BBRSC. Work on the project was supported by a PhD fellowship from the Lundbeck Foundation to CN (2015-3225); the Leducq Foundation (17CVD05), the Novo Nordisk Foundation (NNF21OC0067647, NNF17OC0029724, and NNF19OC0058439), and the Independent Research Fund Denmark to RF; from the Brainstruc center (R155-2015-2666 and R328-2019-546) and a professorship grant (R310-2018-3713) funded by the Lundbeck Foundation and research infrastructure grants from the Carlsberg Foundation (CF15-0821) and the Danish Ministry for Research and Higher Education (EMBION – 5072-00025B) to PN.

## Author contributions

**Caroline Neumann:** Formal analysis; funding acquisition; validation; investigation; visualization; methodology; writing – original draft; writing –

review and editing. **Lena Lindtoft Rosenbæk:** Investigation; visualization; methodology. **Rasmus Kock Flygaard:** Data curation; formal analysis; supervision; visualization; methodology. **Michael Habeck:** Supervision; investigation; methodology. **Jesper Lykkegaard Karlsen:** Software; methodology; project administration. **Yong Wang:** Formal analysis; investigation; visualization; methodology. **Kresten Lindorff-Larsen:** Resources; supervision; investigation; writing – review and editing. **Hans Henrik Gad:** Methodology. **Rune Hartmann:** Resources; supervision; methodology. **Joseph Anthony Lyons:** Supervision; investigation; methodology. **Robert A Fenton:** Conceptualization; resources; formal analysis; supervision; funding acquisition; project administration; methodology; writing – review and editing. **Poul Nissen:** Conceptualization; resources; formal analysis; supervision; funding acquisition; project administration; writing – review and editing.

### Disclosure and competing interests statement

The authors declare that they have no conflict of interest.

## References

- Abraham JA, Murtola T, Schulz R, Pall S, Smith JC, Hess B, Lindahl E (2015) GROMACS: high performance molecular simulations through multi-level parallelism from laptops to supercomputers. *SoftwareX* 1–2: 19–25
- Afonine PV, Poon BK, Read RJ, Sobolev OV, Terwilliger TC, Urzhumtsev A, Adams PD (2018) Real-space refinement in PHENIX for cryo-EM and crystallography. *Acta Crystallogr D Struct Biol* 74: 531–544
- Ares GR, Ortiz PA (2010) Constitutive endocytosis and recycling of NKCC2 in rat thick ascending limbs. *Am J Physiol Renal Physiol* 299: F1193–F1202
- Arroyo JP, Kahle KT, Gamba G (2013) The SLC12 family of electroneutral cation-coupled chloride cotransporters. *Mol Aspects Med* 34: 288–298
- Ben-Yona A, Kanner BI (2009) Transmembrane domain 8 of the  $\{\gamma\}$ -aminobutyric acid transporter GAT-1 lines a cytoplasmic accessibility pathway into its binding pocket. *J Biol Chem* 284: 9727–9732
- Berka K, Hanak O, Sehnal D, Banas P, Navratilova V, Jaiswal D, Ionescu CM, Svobodova Varekova R, Koca J, Otyepka M (2012) MOLEonline 2.0: interactive web-based analysis of biomacromolecular channels. *Nucleic Acids Res* 40: W222–W227
- Blaesse P, Airaksinen MS, Rivera C, Kaila K (2009) Cation-chloride cotransporters and neuronal function. *Neuron* 61: 820–838
- Brown CD, Murer H (1985) Characterization of a Na: K: 2Cl cotransport system in the apical membrane of a renal epithelial cell line (LLC-PK1). *J Membr Biol* 87: 131–139
- Chen N, Vaughan RA, Reith ME (2001) The role of conserved tryptophan and acidic residues in the human dopamine transporter as characterized by site-directed mutagenesis. *J Neurochem* 77: 1116–1127
- Chew TA, Orlando BJ, Zhang J, Latorraca NR, Wang A, Hollingsworth SA, Chen DH, Dror RO, Liao M, Feng L (2019) Structure and mechanism of the cation-chloride cotransporter NKCC1. *Nature* 572: 488–492
- Chi G, Ebenhoch R, Man H, Tang H, Tremblay LE, Reggiano G, Qiu X, Bohstedt T, Liko I, Almeida FG et al (2021a) Phospho-regulation, nucleotide binding and ion access control in potassium-chloride cotransporters. *EMBO J* 40: e107294
- Chi X, Li X, Chen Y, Zhang Y, Su Q, Zhou Q (2021b) Cryo-EM structures of the full-length human KCC2 and KCC3 cation-chloride cotransporters. *Cell Res* 31: 482–484
- Claxton DP, Quick M, Shi L, de Carvalho FD, Weinstein H, Javitch JA, McHaourab HS (2010) Ion/substrate-dependent conformational dynamics of a bacterial homolog of neurotransmitter: Sodium symporters. *Nat Struct Mol Biol* 17: 822–829
- Coleman JA, Green EM, Gouaux E (2016) X-ray structures and mechanism of the human serotonin transporter. *Nature* 532: 334–339
- Colmenero-Flores JM, Martinez G, Gamba G, Vazquez N, Iglesias DJ, Brumos J, Talon M (2007) Identification and functional characterization of cation-chloride cotransporters in plants. *Plant J* 50: 278–292
- Delpire E, Gagnon KB (2011) Kinetics of hyperosmotically stimulated Na-K-2Cl cotransporter in *Xenopus laevis* oocytes. *Am J Physiol Cell Physiol* 301: C1074–C1085
- Delpire E, Gagnon KB (2018) Na(+)-K(+) -2Cl(-) cotransporter (NKCC) physiological function in nonpolarized cells and transporting epithelia. *Compr Physiol* 8: 871–901
- Demian WL, Persaud A, Jiang C, Coyaud E, Liu S, Kapus A, Kafri R, Raught B, Rotin D (2019) The ion transporter NKCC1 links cell volume to cell mass regulation by suppressing mTORC1. *Cell Rep* 27: e1886
- Emsley P, Lohkamp B, Scott WG, Cowtan K (2010) Features and development of coot. *Acta Crystallogr D Biol Crystallogr* 66: 486–501
- Errasti-Murugarren E, Fort J, Bartoccioni P, Diaz L, Pardon E, Carpena X, Espino-Guarch M, Zorzano A, Ziegler C, Steyaert J et al (2019) L amino acid transporter structure and molecular bases for the asymmetry of substrate interaction. *Nat Commun* 10: 1807
- Faham S, Watanabe A, Besserer GM, Cascio D, Specht A, Hirayama BA, Wright EM, Abramson J (2008) The crystal structure of a sodium galactose transporter reveals mechanistic insights into Na<sup>+</sup>/sugar symport. *Science* 321: 810–814
- Fenollar-Ferrer C, Stockner T, Schwarz TC, Pal A, Gotovina J, Hofmaier T, Jayaraman K, Adhikary S, Kudlacek O, Mehdi-pour AR et al (2014) Structure and regulatory interactions of the cytoplasmic terminal domains of serotonin transporter. *Biochemistry* 53: 5444–5460
- Focht D, Neumann C, Lyons J, Eguskiza Bilbao A, Blunck R, Malinauskaite L, Schwarz IO, Javitch JA, Quick M, Nissen P (2021) A non-helical region in transmembrane helix 6 of hydrophobic amino acid transporter MhST mediates substrate recognition. *EMBO J* 40: e105164
- Forrest LR, Rudnick G (2009) The rocking bundle: a mechanism for ion-coupled solute flux by symmetrical transporters. *Physiology (Bethesda)* 24: 377–386
- Forrest LR, Kramer R, Ziegler C (2011) The structural basis of secondary active transport mechanisms. *Biochim Biophys Acta* 1807: 167–188
- Goehring A, Lee CH, Wang KH, Michel JC, Claxton DP, Bacongus I, Althoff T, Fischer S, Garcia KC, Gouaux E (2014) Screening and large-scale expression of membrane proteins in mammalian cells for structural studies. *Nat Protoc* 9: 2574–2585
- Gotfryd K, Boesen T, Mortensen JS, Khelashvili G, Quick M, Terry DS, Missel JW, LeVine MV, Gourdon P, Blanchard SC et al (2020) X-ray structure of LeuT in an inward-facing occluded conformation reveals mechanism of substrate release. *Nat Commun* 11: 1005
- Hartmann AM, Blaesse P, Kranz T, Wenz M, Schindler J, Kaila K, Friauf E, Nothwang HG (2009) Opposite effect of membrane raft perturbation on transport activity of KCC2 and NKCC1. *J Neurochem* 111: 321–331
- Hartmann AM, Nothwang HG (2014) Molecular and evolutionary insights into the structural organization of cation chloride cotransporters. *Front Cell Neurosci* 8: 470
- Hartmann AM, Tesch D, Nothwang HG, Bininda-Emonds OR (2014) Evolution of the cation chloride cotransporter family: ancient origins, gene losses, and subfunctionalization through duplication. *Mol Biol Evol* 31: 434–447
- Hebert SC, Mount DB, Gamba G (2004) Molecular physiology of cation-coupled Cl<sup>-</sup> cotransport: The SLC12 family. *Pflugers Arch* 447: 580–593

- Hoorn EJ, Gritter M, Cuevas CA, Fenton RA (2020) Regulation of the renal NaCl cotransporter and its role in potassium homeostasis. *Physiol Rev* 100: 321–356
- Jaggi AS, Kaur A, Bali A, Singh N (2015) Expanding spectrum of sodium potassium chloride Co-transporters in the pathophysiology of diseases. *Curr Neuropharmacol* 13: 369–388
- Ji W, Foo JN, O’Roak BJ, Zhao H, Larson MG, Simon DB, Newton-Cheh C, State MW, Levy D, Lifton RP (2008) Rare independent mutations in renal salt handling genes contribute to blood pressure variation. *Nat Genet* 40: 592–599
- Joseph D, Pidathala S, Mallela AK, Penmatsa A (2019) Structure and gating dynamics of Na<sup>(+)</sup>/Cl<sup>(-)</sup> coupled neurotransmitter transporters. *Front Mol Biosci* 6: 80
- Kalayil S, Schulze S, Kuhlbrandt W (2013) Arginine oscillation explains Na<sup>+</sup> independence in the substrate/product antiporter CaiT. *Proc Natl Acad Sci U S A* 110: 17296–17301
- Kantcheva AK, Quick M, Shi L, Winther AM, Stolzenberg S, Weinstein H, Javitch JA, Nissen P (2013) Chloride binding site of neurotransmitter sodium symporters. *Proc Natl Acad Sci U S A* 110: 8489–8494
- Kazmier K, Sharma S, Quick M, Islam SM, Roux B, Weinstein H, Javitch JA, McHaourab HS (2014) Conformational dynamics of ligand-dependent alternating access in LeuT. *Nat Struct Mol Biol* 21: 472–479
- Khafizov K, Perez C, Koshy C, Quick M, Fendler K, Ziegler C, Forrest LR (2012) Investigation of the sodium-binding sites in the sodium-coupled betaine transporter BetP. *Proc Natl Acad Sci U S A* 109: E3035–E3044
- Kinne R, Kinne-Saffran E, Scholermann B, Schutz H (1986) The anion specificity of the sodium-potassium-chloride cotransporter in rabbit kidney outer medulla: studies on medullary plasma membranes. *Pflugers Arch* 407: S168–S173
- Korkhov VM, Holy M, Freissmuth M, Sitte HH (2006) The conserved glutamate (Glu136) in transmembrane domain 2 of the serotonin transporter is required for the conformational switch in the transport cycle. *J Biol Chem* 281: 13439–13448
- Koumangoye R, Bastarache L, Delpire E (2021) NKCC1: newly found as a human disease-causing ion transporter. *Function (Oxf)* 2: zqaa028
- Krishnamurthy H, Piscitelli CL, Gouaux E (2009) Unlocking the molecular secrets of sodium-coupled transporters. *Nature* 459: 347–355
- Krishnamurthy H, Gouaux E (2012) X-ray structures of LeuT in substrate-free outward-open and apo inward-open states. *Nature* 481: 469–474
- Laursen L, Severinsen K, Kristensen KB, Periole X, Overby M, Muller HK, Schiott B, Sinning S (2018) Cholesterol binding to a conserved site modulates the conformation, pharmacology, and transport kinetics of the human serotonin transporter. *J Biol Chem* 293: 3510–3523
- Li J, Tajkhorshid E (2009) Ion-releasing state of a secondary membrane transporter. *Biophys J* 97: L29–L31
- Li J, Zhao Z, Tajkhorshid E (2019) Locking two rigid-body bundles in an outward-facing conformation: the ion-coupling mechanism in a LeuT-fold transporter. *Sci Rep* 9: 19479
- Liu S, Chang S, Han B, Xu L, Zhang M, Zhao C, Yang W, Wang F, Li J, Delpire E et al (2019) Cryo-EM structures of the human cation-chloride cotransporter KCC1. *Science* 366: 505–508
- Lytle C, McManus TJ, Haas M (1998) A model of Na-K-2Cl cotransport based on ordered ion binding and glide symmetry. *Am J Physiol* 274: C299–C309
- Malinauskaitė L, Quick M, Reinhard L, Lyons JA, Yano H, Javitch JA, Nissen P (2014) A mechanism for intracellular release of Na<sup>+</sup> by neurotransmitter/sodium symporters. *Nat Struct Mol Biol* 21: 1006–1012
- Markadieu N, Delpire E (2014) Physiology and pathophysiology of SLC12A1/2 transporters. *Pflugers Arch* 466: 91–105
- Nakane T, Kimanius D, Lindahl E, Scheres SH (2018) Characterisation of molecular motions in cryo-EM single-particle data by multi-body refinement in RELION. *Elife* 7: e36861
- Payne JA (2012) Molecular operation of the cation chloride cotransporters: Ion binding and inhibitor interaction. *Curr Top Membr* 70: 215–237
- Penmatsa A, Wang KH, Gouaux E (2013) X-ray structure of dopamine transporter elucidates antidepressant mechanism. *Nature* 503: 85–90
- Perez C, Koshy C, Yildiz O, Ziegler C (2012) Alternating-access mechanism in conformationally asymmetric trimers of the betaine transporter BetP. *Nature* 490: 126–130
- Punjani A, Rubinstein JL, Fleet DJ, Brubaker MA (2017) cryoSPARC: algorithms for rapid unsupervised cryo-EM structure determination. *Nat Methods* 14: 290–296
- Reid MS, Kern DM, Brohawn SG (2020) Cryo-EM structure of the potassium-chloride cotransporter KCC4 in lipid nanodiscs. *Elife* 9: e52505
- Rohou A, Grigorieff N (2015) CTFIND4: fast and accurate defocus estimation from electron micrographs. *J Struct Biol* 192: 216–221
- Rosenbaek LL, Kortenoeven ML, Aroankins TS, Fenton RA (2014) Phosphorylation decreases ubiquitylation of the thiazide-sensitive cotransporter NCC and subsequent clathrin-mediated endocytosis. *J Biol Chem* 289: 13347–13361
- Russell JM (2000) Sodium-potassium-chloride cotransport. *Physiol Rev* 80: 211–276
- Scheres SH (2012) RELION: implementation of a Bayesian approach to cryo-EM structure determination. *J Struct Biol* 180: 519–530
- Sen N, Shi L, Beuming T, Weinstein H, Javitch JA (2005) A pincer-like configuration of TM2 in the human dopamine transporter is responsible for indirect effects on cocaine binding. *Neuropharmacology* 49: 780–790
- Shaffer PL, Goehring A, Shankaranarayanan A, Gouaux E (2009) Structure and mechanism of a Na<sup>+</sup>-independent amino acid transporter. *Science* 325: 1010–1014
- Shahsavari A, Stohler P, Bourenkov G, Zimmermann I, Siegrist M, Guba W, Pinard E, Sinning S, Seeger MA, Schneider TR et al (2021) Structural insights into the inhibition of glycine reuptake. *Nature* 591: 677–681
- Shaikh SA, Tajkhorshid E (2010) Modeling and dynamics of the inward-facing state of a Na<sup>+</sup>/Cl<sup>-</sup> dependent neurotransmitter transporter homologue. *PLoS Comput Biol* 6: e1000905
- Simon DB, Karet FE, Hamdan JM, DiPietro A, Sanjad SA, Lifton RP (1996a) Bartter’s syndrome, hypokalaemic alkalosis with hypercalciuria, is caused by mutations in the Na-K-2Cl cotransporter NKCC2. *Nat Genet* 13: 183–188
- Simon DB, Nelson-Williams C, Bia MJ, Ellison D, Karet FE, Molina AM, Vaara I, Iwata F, Cushner HM, Koolen M et al (1996b) Gitelman’s variant of Bartter’s syndrome, inherited hypokalaemic alkalosis, is caused by mutations in the thiazide-sensitive Na-Cl cotransporter. *Nat Genet* 12: 24–30
- Somasekharan S, Tanis J, Forbush B (2012) Loop diuretic and ion-binding residues revealed by scanning mutagenesis of transmembrane helix 3 (TM3) of Na-K-Cl cotransporter (NKCC1). *J Biol Chem* 287: 17308–17317
- Sucic S, Paczkowski FA, Runkel F, Bonisch H, Bryan-Lluka LJ (2002) Functional significance of a highly conserved glutamate residue of the human noradrenaline transporter. *J Neurochem* 81: 344–354
- Tavoulari S, Margheritis E, Nagarajan A, DeWitt DC, Zhang YW, Rosado E, Ravera S, Rhoades E, Forrest LR, Rudnick G (2016) Two Na<sup>+</sup> sites control conformational change in a neurotransmitter transporter homolog. *J Biol Chem* 291: 1456–1471
- Turner RJ, George JN (1988) Ionic dependence of bumetanide binding to the rabbit parotid Na/K/Cl cotransporter. *J Membr Biol* 102: 71–77

- Warmuth S, Zimmermann I, Dutzler R (2009) X-ray structure of the C-terminal domain of a prokaryotic cation-chloride cotransporter. *Structure* 17: 538–546
- Weyand S, Shimamura T, Yajima S, Suzuki S, Mirza O, Krusong K, Carpenter EP, Rutherford NG, Hadden JM, O'Reilly J et al (2008) Structure and molecular mechanism of a nucleobase-cation-symport-1 family transporter. *Science* 322: 709–713
- Williams CJ, Headd JJ, Moriarty NW, Prisant MG, Videau LL, Deis LN, Verma V, Keedy DA, Hintze BJ, Chen VB et al (2018) MolProbity: more and better reference data for improved all-atom structure validation. *Protein Sci* 27: 293–315
- Xie Y, Chang S, Zhao C, Wang F, Liu S, Wang J, Delpire E, Ye S, Guo J (2020) Structures and an activation mechanism of human potassium-chloride cotransporters. *Sci Adv* 6: eabc5883
- Yamashita A, Singh SK, Kawate T, Jin Y, Gouaux E (2005) Crystal structure of a bacterial homologue of Na<sup>+</sup>/Cl<sup>-</sup>-dependent neurotransmitter transporters. *Nature* 437: 215–223
- Yan R, Zhang Y, Li Y, Xia L, Guo Y, Zhou Q (2020) Structural basis for the recognition of SARS-CoV-2 by full-length human ACE2. *Science* 367: 1444–1448
- Yang X, Wang Q, Cao E (2020) Structure of the human cation-chloride cotransporter NKCC1 determined by single-particle electron cryo-microscopy. *Nat Commun* 11: 1016
- Zhang YW, Tavoulari S, Sinning S, Aleksandrova AA, Forrest LR, Rudnick G (2018) Structural elements required for coupling ion and substrate transport in the neurotransmitter transporter homolog LeuT. *Proc Natl Acad Sci U S A* 115: E8854–E8862
- Zhang S, Zhou J, Zhang Y, Liu T, Friedel P, Zhuo W, Somasekharan S, Roy K, Zhang L, Liu Y et al (2021) The structural basis of function and regulation of neuronal cotransporters NKCC1 and KCC2. *Commun Biol* 4: 226
- Zhao Y, Terry D, Shi L, Weinstein H, Blanchard SC, Javitch JA (2010) Single-molecule dynamics of gating in a neurotransmitter transporter homologue. *Nature* 465: 188–193
- Zhao Y, Roy K, Vidossich P, Cancedda L, De Vivo M, Forbush B, Cao E (2022) Structural basis for inhibition of the cation-chloride cotransporter NKCC1 by the diuretic drug bumetanide. *Nat Commun* 13: 2747
- Zimanyi CM, Guo M, Mahmood A, Hendrickson WA, Hirsh D, Cheung J (2020) Structure of the regulatory cytosolic domain of a eukaryotic potassium-chloride cotransporter. *Structure* 28: 1051–1060



**License:** This is an open access article under the terms of the [Creative Commons Attribution-NonCommercial-NoDerivs](https://creativecommons.org/licenses/by-nc-nd/4.0/) License, which permits use and distribution in any medium, provided the original work is properly cited, the use is non-commercial and no modifications or adaptations are made.